A non-interleaved round beam lattice for light sources

Ilya Agapov, Reinhard Brinkmann, Joachim Keil, and Rainer Wanzenberg
DESY, Notkestrasse 85, 22607, Hamburg, Germany

A conceptual design and performance of a round beam lattice for synchrotron light sources based on the phase space exchange principle and the non-interleaved sextupole distribution is presented. Optics design is performed for an approximately 30 pm emittance 6 GeV machine of 2300 m circumference which combines cells with and without straight sections for the insertion devices.

I. INTRODUCTION

Synchrotron light sources operate with flat beams, but round beams might be desirable for mitigating the effect of intra-beam scattering (IBS) [1, 2] or for improving the optical properties of the produced undulator radiation [3]. There are several approaches to producing round beams in synchrotrons [4], the usual one consisting in exploiting the natural coupling of the machine. The coupling is typically a small undesired effect in a synchrotron and has to be amplified by working on a resonance [5]. Resonances are by definition areas of sensitive and irregular motion. Small changes to the tune could strongly affect the emittance; optics measurement and correction can be extremely non-trivial. Thus, another approach consists in introducing full coupling non-resonantly. Working with a fully coupled optics is difficult and multiple parametrizations of the optical functions are in use (see e.g. [6–9]). A simple way to introduce full coupling is to flip the horizontal and vertical modes of betatron oscillation a finite number of times in the ring so that on average the number of oscillations in both planes is roughly equal; the coupling in this case is localized and affects only integral characteristics such as the emittance. One does not need to resort to coupled beam envelope formalism for optics design, matching etc. It is technically simplest to implement just one mode flip per revolution; the concept has been studied for round beam production both theoretically [10–13] and experimentally [14] and is known as the "Möbius accelerator". A round beam lattice with two flips is employed for the VEPP2000 collider [15] for reasons of improving the luminosity.

The new generation of synchrotron light sources ([16–19]) push down the beam emittance by employing the multi-bend achromat (MBA) concept [20–24]. In such lattices strong focusing produces large negative chromaticity, and the sextupoles needed to compensate it are typically strong. This, in turn, has a strong impact on the dynamic aperture and the momentum acceptance. A usual path to improving the dynamic aperture is to arrange sextupoles so that their detrimental effects cancel to the highest possible order. One of the simplest schemes to do so is to arrange for a phase advance of π in both planes between adjacent sextupoles of same polarity. Such scheme is referred to as the non-interleaved scheme. The nonlinear effects of sextupoles in the thin-lense on-momentum approximation cancel, and a very large dynamic aperture is possible [25, 26].

In this paper we explore the combination of the two approaches – phase space flip and the non-interleaved sextupole scheme – for the design of a synchrotron light source lattice. The optics approach and conceptual lattice design for the PETRA ring ([27]) upgrade based on this scheme is presented in Section II. Nonlinear properties of the non-interleaved optics and a study of resonances in a simplified model of the phase space exchange lattice are presented in Section III. After that, the acceptance of the lattice is presented in section IV.

The parameters of the lattice presented here are such that it is a possible lattice for the upgrade of the PETRA III light source at DESY [27–29]. Several lattice types are under consideration, and the lattice discussed here falls into a more conservative category with about 30 pm rad bare lattice emittance. More aggressive designs with down to 10 pm rad emittance are also being considered, and the lattice selection process in currently ongoing. The projected parameters for PETRA IV are shown in Table I.

Parameter	**PETRA IV**
Beam energy	6 GeV
Circumference	2304 m
No. bunches	80 - 4000
Emittance $\varepsilon_x, \varepsilon_y$	$10-30$, $10-30$ pm $\cdot$ rad
Energy spread	$0.7-1.5\cdot10^{-3}$ (4.2 - 9 MeV)
Bunch length	10-50 ps (rms)
Beam current	100 -200 mA
β-function at IDs	1 -7 m

TABLE I: Target PETRA IV parameters.

II. LATTICE

A. Principles

The first principle exploited in the presented lattice is using different cell types in different octants. PETRA III has been converted into a light source from an originally high energy physics collider ring, which defines its geometry:

FIG. 1: Layout of the PETRA III/IV infrastructure. Positions of the phase space exchange sections follwoing the two octants with insertion devices are shown with arrows.

eight octants linked by eight straight sections of approx. 100 or 60 m length, with only one octant initially occupied by the double-bend achromats (DBAs), and the rest by FODO cells without the insertion devices. Parts of two additional octants were converted to DBA optics during an extension project ([28])). The proposed facility layout for the next upgrade is shown in Figure 1. The specific geometry can be made use of in the lattice design. In the lattice presented here, two octants are occupied by cells with insertion devices, and the rest of the ring has optics – long achromats – where no place for insertions is foreseen.

The second principle is the non-interleaved sextupole arrangement, mentioned before. And finally, two phase space exchange sections make it possible to use only horizontally focusing sextupoles to correct the chromaticity in both planes simultaneously. If we call the parts of the ring between the phase space exchange sections A and B, then correcting the ring to zero chromaticity requires

$$\xi_x^A + \xi_y^B = 0 \quad \xi_y^A + \xi_x^B = 0 \tag{1}$$

The chromaticity correction can be distributed over various cell types, as discussed further. The phase space exchange can be installed in any of the long straight sections, one possible choice is indicated in Figure 1 with arrows. The lattice on which the calculations are based has periodicity two, with one undulator octant and three long achromat octants per half of the ring.

B. Non-interleaved undulator cells

An optics solution employed at all modern light sources that minimizes the emittance ([30, 31]) while providing zero (or close to zero) dispersion is the Multi-Bend Achromat (MBA). A 23 m long six bend achromat (6BA) cell, with π phase advance between the two focusing sextupoles, is used in the present lattice. The cell optical functions are shown in Figure 2. An arc consists of 9 such cells. The cell phase advances are chosen such that the phase advances per arc are integer multiples of 2π in both planes. The chromaticities of the cell depending on the strength of the focusing sextupole pair are shown in Table II.

C. Long achromats

In the arcs without the insertion devices, a simpler optics is possible. The arc is made of 15 12 m long unit cells and two dispersion suppressor cells at the arc ends. The optical functions of the cell are shown in Figure 3. The lattice is a

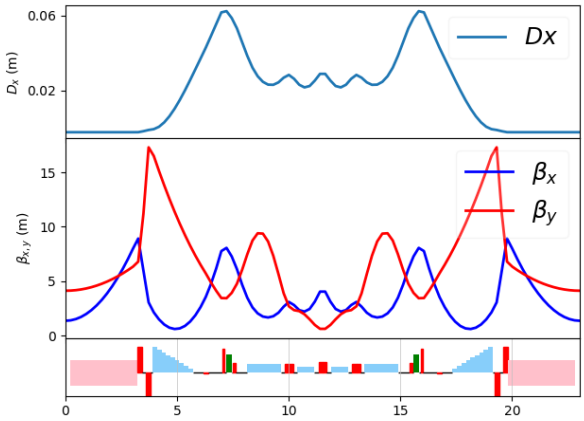

FIG. 2: Possible cell optics for the insertion. The four central bends are combined-function magnets.

modification of a 6BA cell with vertically focusing combined function magnets, a common approach in low-emittance lattices. Strong defocusing in combined-function magnets improves the emittance ([32]), but can potentially lead to the longitudinal partition shifting towards zero, resulting in a large natural energy spread or even longitudinal instability. In order to reasonably balance the transverse and longitudinal partition shifts we also introduced three horizontally focusing combined function magnets for better control of the partition number distribution. The optical functions of the octant are shown in Figure 4. The chromaticities of the cell as a function of the strength of the focusing sextupole pair are shown in Table II.

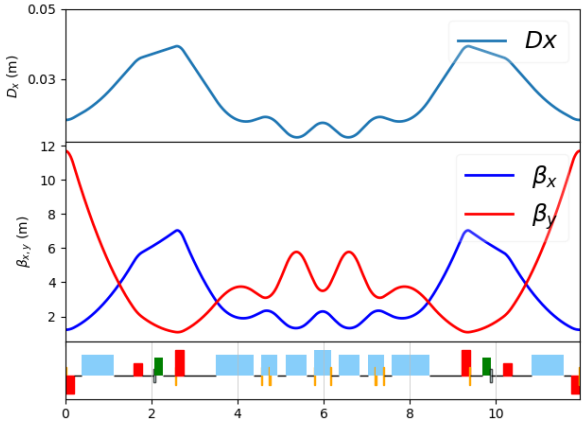

FIG. 3: Optical functions in a cell of the arc (octant) without the undulator insertions.

D. Phase space exchange

The long straight sections are realized with triplet optics. In addition two of the straights have a phase space exchange section. It is a π phase advance FODO section with the normal quadrupole component changed to skew quadrupole component, which has the 4×4 transfer matrix

$$\mathcal{R} = \begin{bmatrix} 0 & 0 & 1 & 0 \\ 0 & 0 & 0 & 1 \\ 1 & 0 & 0 & 0 \\ 0 & 1 & 0 & 0 \end{bmatrix}$$

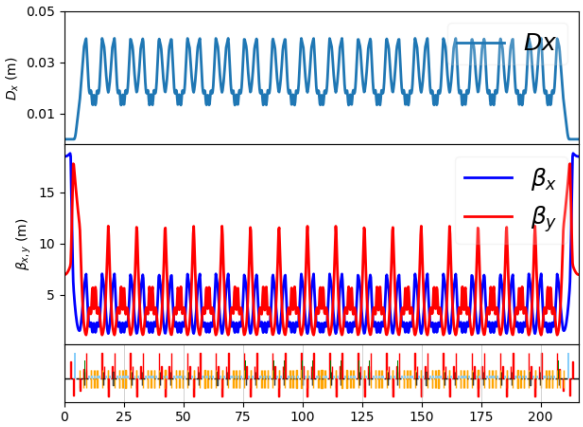

FIG. 4: Optical functions in the arc (octant) without the undulator insertions.

	Parameter	Natural	ξ_x=0	$\xi_x + \xi_y$=0
Cell 1	m_s (T m^{-2})	0	34	85
	ξ_x	-2.6	0	5
	ξ_y	-2.4	-3	-5
	$\xi_x + \xi_y$	-5	-3	0
Cell 2	m_s (T m^{-2})	0	22	65
	ξ_x	-0.8	0	1.6
	ξ_y	-1.1	-1.2	-1.6
	$\xi_x + \xi_y$	-1.9	-1.2	0

TABLE II: Cell chromaticities vs. sextupole strength for the undulator cell (Cell 1) and for the cell in the arcs without insertions (Cell 2).

The same section has an identity transform when the skew quadrupole components are replaced again by normal components, e.g. by means of rotation. The optics of such section is shown in Figure 5. The phase advances of the long straight sections are approximately 2π, with the fractional phase advance part used for tune matching, and the chromaticities bewteen -2 and -3 units in both planes for all three types of long straight sections.

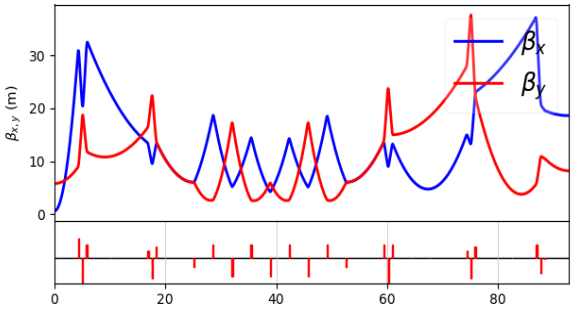

FIG. 5: Straight section with the triplet optics including the skew FODO phase space exchange section. The optical functions are plotted for the quadrupoles set in the normal (not skew) mode.

E. Lattice parameters

The Mais-Ripken coupled lattice functions [8] of the ring are shown in Figure 6 (for discussion of coupled lattice functions see e.g. [9]).

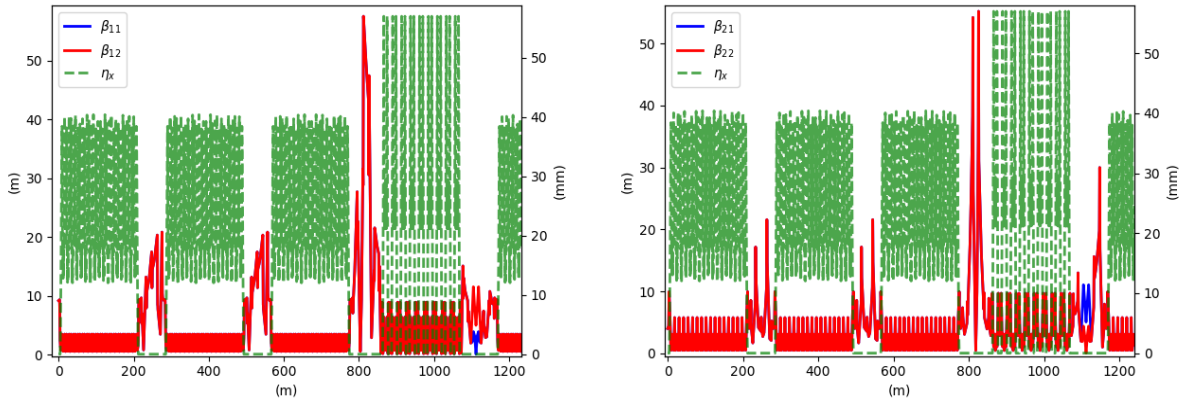

FIG. 6: Mais-Ripken optical functions of the full lattice. Half of the ring (four octants) is shown.

The lattice parameters are presented in Table III. Note that the insertion devices have a significant impact on the equilibrium emittance and the energy spread. So, if all (short) straight sections in the two octants are occupied by 23 mm period undulators with 0.7 T rms field, the emittance will be reduced by more than a factor of two. Also note that the effect of a small longitudinal partition number (approx 0.1) on the energy spread is mitigated by undulators or damping wigglers. This follows from

$$\left(\frac{\sigma_{E,wig}}{\sigma_{E,0}}\right)^2 = \frac{1+\frac{\mathcal{I}_{3,wig}}{\mathcal{I}_{3,0}}}{1+\frac{\mathcal{I}_{2,wig}}{\mathcal{I}_{2,0}}}\frac{j_{z,0}}{j_{z,wig}} \tag{2}$$

where $\mathcal{I}_2$ and $\mathcal{I}_3$ are the radiation integrals and j_z the longitudinal partition number defined in the usual way [33], and the subscripts indicate the values with and without damping wigglers.

Parameter	**Value**
Beam energy	6 GeV
Emittance, bare lattice (hor., vert.)	28 pm, 28 pm
Emittance, 0.7T (rms) IDs	12 pm, 12 pm
Energy spread, bare lattice	$2.6 \cdot 10^{-3}$
Energy spread, 0.7T IDs	$1.0 \cdot 10^{-3}$
Integer tunes	123 , 123
Natural chromaticity	-188 , -188

TABLE III: Lattice parameters, collective effects neglected.

The question of dynamic aperture and momentum acceptance of the lattice is discussed in the next Sections.

III. NONLINEAR DYNAMICS

A. Nonlinear dynamics in non-interleaved lattices

In the non-interleaved optics sextupole kicks separated by π phase advance cancel exactly (neglecting the sextupole length effect which is small in practice), and the on-momentum dynamic aperture is large without any need for further nonlinearity cancellation. The higher-order chromaticies, however, are hard to compensate (see e.g. [34]) and become a limiting factor in such lattices. In the lattice presented here, the distribution of sextupole strengths between two types of octants becomes an additional knob for higher-order chromaticity control. In Figure 7 sums of second-order chromaticities for the two types of cells in the ring are shown. The calculations were done with the PTC

module integrated with MADX [35, 36]. In terms of second-order chromaticity cancellation, neither distributing the correction between two types of cells equally, nor having all correction done in the no-undulator cells is optimal. The region chosen for tracking studies in this work is highlighted in red and corresponds to somewhat redistributing the linear chromaticity correction towards the undulator cells, with the sextupole strengths in all cells larger than what is required for cell chromaticity compensation due to the additional contribution of the long straight sections (c.f. Table II. Note that the second-order chromaticity of the ring is not a simple sum of cell chromaticities (see [34]), and the higher-order terms play an important role, so the second-order cell analysis gives only a starting point for further optimization.

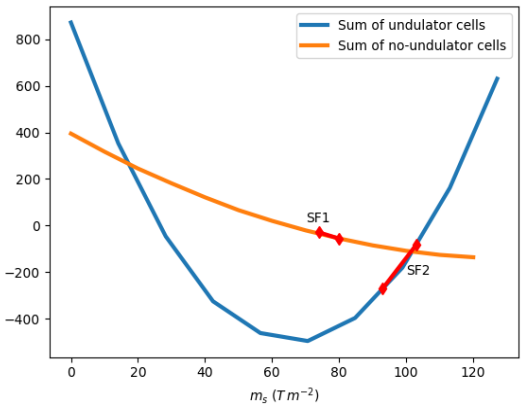

FIG. 7: Sums of second-order chromaticities (horizontal plus vertical) over the total number of cells in the ring. The horizontal axis shows sextupole strength in two different cell types, and the regions highlighted in red correspond to the ranges of strengths for linear chromaticity compensation used in the tracking studies.

B. Study of stability domain in a simplified phase space exchange model

Although various nonlinear characteristics of particle motion could be derived perturbatively to lowest orders, they are often represented by entangled expressions and cannot provide quantitative description of the figures of merit such as the dynamic aperture. The situation becomes even more complicated when coupling is introduced, so to proceed further with the discussion of the effect of phase space exchange on the dynamics, a simplified model is introduced. Following the usual approach, we model a one turn map as a linear map plus a nonlinear kick. In addition, the phase space exchange is introduced. Consider first the sextupole nonlinearity, modeled by the combination of linear, sextupole, and phase space exchange maps applied two times as follows

$$\mathcal{M}_3 = \mathcal{M}_S \cdot \mathcal{M}_{TW} \cdot \mathcal{M}_{LIN} \cdot \mathcal{M}_S \cdot \mathcal{M}_{TW} \cdot \mathcal{M}_{LIN} \tag{3}$$

where the linear part is a 4×4 matrix

$$\mathcal{M}_{LIN} : \begin{pmatrix} \mathcal{M}_{LIN,X} & 0 \\ 0 & \mathcal{M}_{LIN,Y} \end{pmatrix} \tag{4}$$

$$\mathcal{M}_{LIN,X,Y} : \begin{pmatrix} \cos(2\pi\mu_{x,y}) & \sin(2\pi\mu_{x,y}) \\ -\sin(2\pi\mu_{x,y}) & \cos(2\pi\mu_{x,y}) \end{pmatrix} \tag{5}$$

the phase space exchange part is a 4×4 matrix

$$\mathcal{M}_{TW} : \begin{pmatrix} 0 & \mathcal{I} \\ \mathcal{I} & 0 \end{pmatrix} \tag{6}$$

with $\mathcal{I}$ the identity, and the thin lens sextupole map is

$$\mathcal{M}_S : \begin{pmatrix} x \\ x' \\ y \\ y' \end{pmatrix} \to \begin{pmatrix} x \\ x' - m(x^2 - y^2) \\ y \\ y' + 2mxy \end{pmatrix} \tag{7}$$

This is a greatly simplified model of a phase space exchange lattice with the tunes $\mu_x + \mu_y$ and a residual sextupole aberration averaged over half of the ring. The longitudinal degree of freedom is neglected. When the phase space exchange is removed from the map, it becomes a usual toy model of Hénon-Heiles type [37] used in studying nonlinear dynamics is storage rings

$$\tilde{\mathcal{M}}_3 = \mathcal{M}_S \cdot \mathcal{M}_{LIN} \cdot \mathcal{M}_S \cdot \mathcal{M}_{LIN} \tag{8}$$

We will study the stability of such maps as a function of the phase advances of the linear part. The nonlinearity parameter m is not essential since the oscillation amplitudes can be always rescaled, so m will be arbitrarily fixed to 0.5. In Figure 8 stability diagrams of the maps $\tilde{\mathcal{M}}_3$ and $\mathcal{M}_3$ depending on the phase advances are shown. The diagrams are produced as follows: tracking is done for a certain sufficiently large initial x and y for 10^4 turns. The oscillations are either bounded or grow very rapidly. The initial phase advances for which the oscillations are bounded are plotted in the diagram. A sufficiently small initial condition will produce stable motion for all phase advances, while a sufficiently large initial condition will produce a motion which is unstable for all phase advances, so the value $x_0 = y_0 = 0.5$ is representative of the regime where stable and unstable domains are clearly visible. The effect of taking a different initial condition is mainly quantitative, the stability domain is larger for smaller initial conditions, while the general resonance picture remains. In the uncoupled case the unstable resonances are seen, with integer and third integer being the strongest. In the coupled case the diagram becomes almost one dimensional (if the projection on the diagonal is considered), and the instability domains correspond to the resonant conditions $2\mu_x + 2\mu_y = 2/3$, $2\mu_x + 2\mu_y = 4/3$, $2\mu_x + 2\mu_y = 1$ and $2\mu_x + 2\mu_y = 0$.

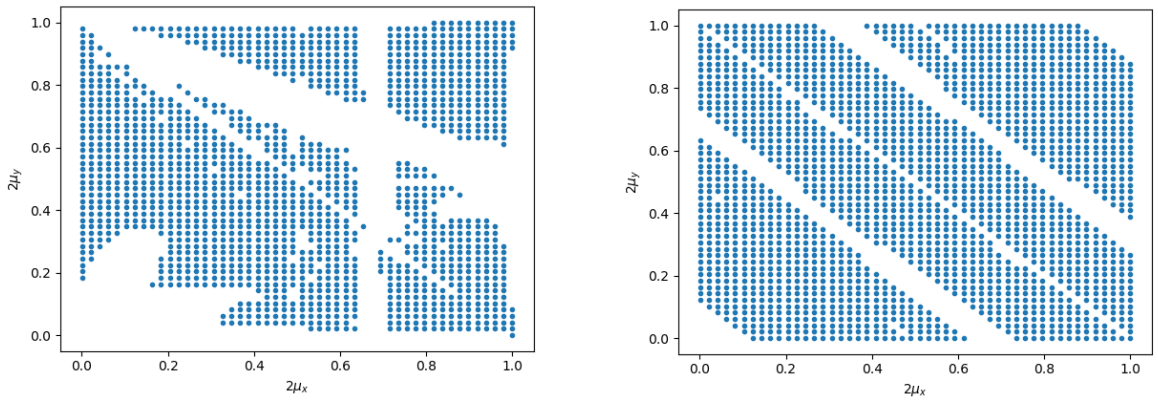

(a) $\tilde{\mathcal{M}}_3$ (b) $\mathcal{M}_3$

FIG. 8: Stability diagrams of third-order maps, $x_0 = y_0 = 0.5$.

Next, some examples of phase space portraits are shown in Figures 9 and 10. Trajectories with different initial amplitudes in the horizontal direction are shown. While for the uncoupled case one observes the well known picture of transition to instability with resonant islands and chaotic layers, the geometry of the coupled motion is more complex. Multitude of geometric patterns can be produced in that way.

Fourth-order nonlinearities have significant impact on beam dynamics, so we proceed to analyze the effect of the octupole nonlinearity with model maps

$$\mathcal{M}_4 = \mathcal{M}_O \cdot \mathcal{M}_{TW} \cdot \mathcal{M}_{LIN} \cdot \mathcal{M}_O \cdot \mathcal{M}_{TW} \cdot \mathcal{M}_{LIN} \tag{9}$$

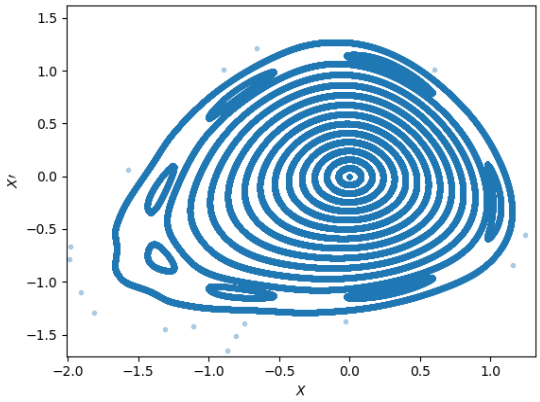

FIG. 9: Phase space portrait of $\tilde{\mathcal{M}}_3$ (third-order uncoupled map), $\mu_x = \mu_y = 1/6$.

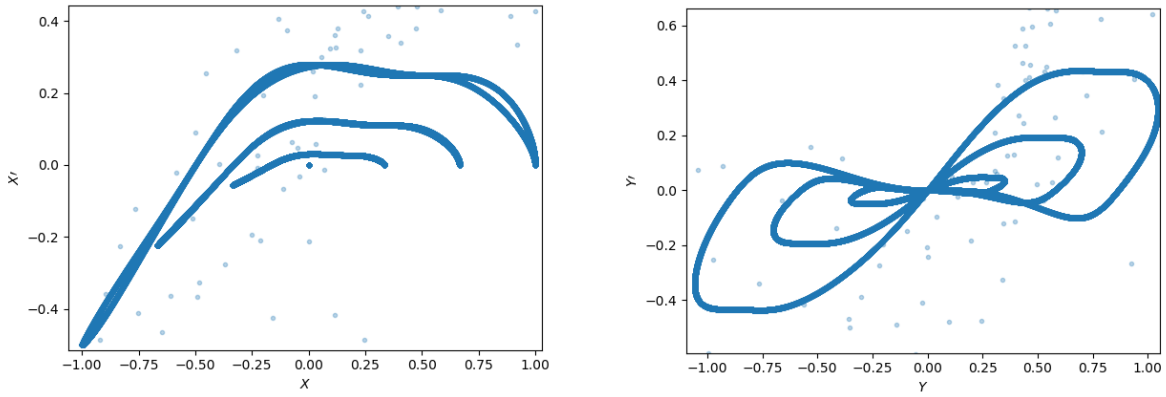

(a) $\tilde{\mathcal{M}}_3$ (b) $\mathcal{M}_3$

FIG. 10: Phase space portraits of $\mathcal{M}_3$ (third-order coupled map), $\mu_x = \mu_y = 1/4$.

and

$$\tilde{\mathcal{M}}_4 = \mathcal{M}_O \cdot \mathcal{M}_{LIN} \cdot \mathcal{M}_O \cdot \mathcal{M}_{LIN} \tag{10}$$

where

$$\mathcal{M}_O : \begin{pmatrix} x \\ x' \\ y \\ y' \end{pmatrix} \rightarrow \begin{pmatrix} x \\ x' + m_O(\frac{x^3}{3} - xy^2) \\ y \\ y' + m_O(\frac{y^3}{3} - x^2 y) \end{pmatrix} \tag{11}$$

with m_O being the octupole strength, set to 1.0 in calculations. The phase space portraits in this case are shown in Figure 11. Interestingly, two octupole kicks cancel out over one revolution, and the horizontal dynamics does not couple into vertical. The phase space geometry in the two cases is similar. This can be also inferred from the symmetry of the octupole field with respect to interchanging x and y. The stability diagrams in both cases are also similar, and shown in Figure 12.

To summarize the results from the simplified model, the phase space exchange alters the geometry of the phase space, but does not significantly reduce the regions of stability in the tune and in the amplitude space.

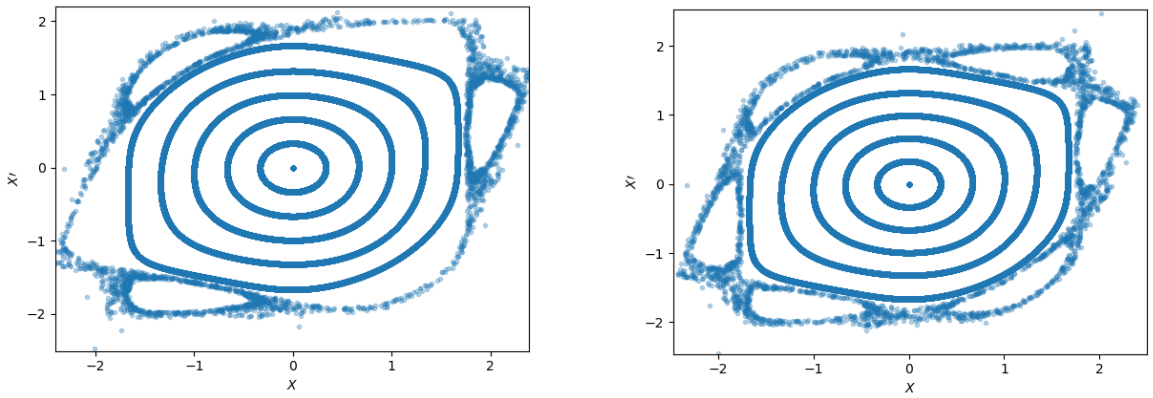

(a) $\tilde{\mathcal{M}}_4$ (b) $\mathcal{M}_4$

FIG. 11: Phase space portraits of fourth-order maps, $\mu_x = \mu_y = 0.21$.

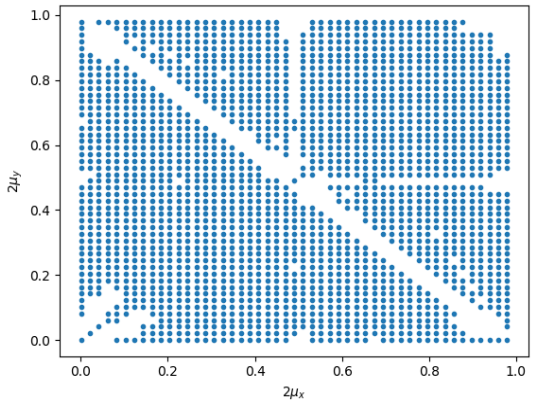

FIG. 12: Stability diagram of $\mathcal{M}_4$, $x_0 = 0.5$, $y_0 = 0.5$, $m_O = 1.0$.

IV. ACCEPTANCE OF THE LATTICE

Analytical estimates and simplified models provide qualitative description of lattice behavior and strategies for compensating nonlinear aberrations. Quantitative performance estimates and optimization is always performed with particle tracking, which can be a time and CPU consuming procedure for a machine like PETRA. A procedure involving extensive parameter scans or advanced optimization is inevitable for a technical design of a facility. In this paper we present a conceptual design, and extensive optimization is avoided; the parameters are selected based on principles provided in the previous sections. Moreover, already relatively small alignment errors can influence the acceptance of MBA machines. Both the optimization and the tolerance study are subjects of separate work and are not addressed here.

The cell phase advances are chosen to fulfil the achromat condition: the 9 undulator cells per arc make the phase advances of 15 and 8 in units of 2π in horizontal and vertical planes respectively, while the rest of the ring is such that the horizontal and vertical phase advances of the 17 cells per arc sum up to 13 and 12. However, the exact fulfillment of this condition is not important for non-interleaved lattices since geometric aberrations are already canceled to a high degree of precision regardless of the cell phase advance. This leaves additional freedom for selecting the beta function in the undulator insertions.

In Figure 13 the lattice acceptance is shown for fractional tunes $Q_x = 0.76$ and $Q_y = 0.76$, and linear chromaticities $\xi_x = 0$ and $\xi_y = 0$. A large dynamic aperture (approx. 4.5 mm mrad or 15 mm at β_x=50 m horizontally, and approx. 2.5 mm mrad or 11 mm at β_y=50 m vertically) and a momentum acceptance of approx. 1.6% can be observed. The tune footprint is shown in Figure 14, the integer, $Q_x = 2/3$, $Q_y = 2/3$ and the $Q_x + Q_y = 4/3$ resonances confining

the tune footprint.

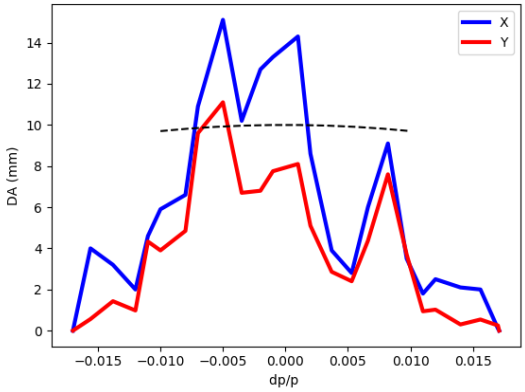

FIG. 13: Dynamic aperture vs. momentum offset, β_x=50 m, β_y=50 m. Limitation due to the path lengthening effect for a typical RF setting is shown as a dashed line.

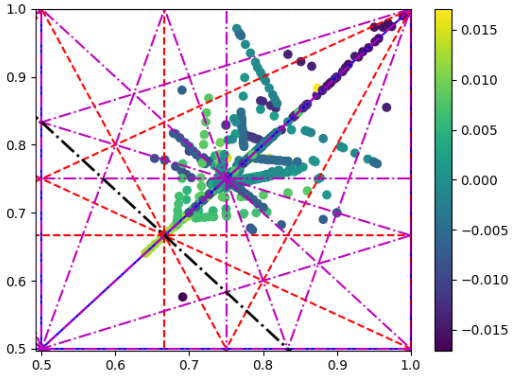

FIG. 14: Tune diagram for horizontal, vertical, and longitudinal degrees of freedom, color-coded by momentum offset.

A known feature of low momentum compaction lattices (the present lattice has $\alpha_C = 4 \cdot 10^{-5}$) is the strong coupling of transverse oscillations into the longitudinal dimension due to the path lengthening effect. The shift of the path length per revolution is given to first order by [38, 39]

$$\Delta C = -2\pi \left(J_X \xi_x + J_Y \xi_y \right) \tag{12}$$

where J_X and J_Y are betatron actions, and ξ_x and ξ_y are the chromaticities. Longitudinal oscillations are thus excited for particles with large transverse offsets, which limits the dynamic aperture. For a 100 MHz RF system with 10 MV total voltage, the limitation is about 2 mm mrad as shown in Figure 13.

V. CONCLUSION

We presented a conceptual design of a non-interleaved round beam lattice for electron light sources. Its dynamic aperture and momentum acceptance have been analyzed. It is easy to implement in case round beam operation is the preferred mode. The dynamic aperture of the lattice is large, and is limited by the synchro-betatron coupling driven by the path lengthening effect. The momentum acceptance is somewhat restrictive, a situation common for non-interleaved lattices, but can be to a certain extent controlled by redistributing the chromaticity correction between

ring octants. This type of lattice can potentially be used for other types of electron storage rings such as lepton colliders.

---

[1] A. Piwinski, Intra-beam scattering, in Proceedings of the 9th International Conference on High Energy Accelerators, Stanford, CA, 1974
[2] J. Bjorken and S. Mtingwa, Intrabeam Scattering, Part. Accel. 13, 115 (1983)
[3] K.-J. Kim, Optical and power characteristics of synchrotron radiation sources, Optical Engineering 34(2), 342 - 352 (1995)
[4] P. Kuske, Round beam related challenges in storage ring light sources, in Proceedings of the Future Light Source 2018 workshop, Shanghai, China (2018)
[5] G. Guignard, Betatron coupling and related impact of radiation, Phys. Rev. E 51, 6, 6104-6118 (1995)
[6] D. A. Edwards and L. C. Teng, Parametrization of coupled motion in periodic systems, IEEE Trans. Nucl. Sci. 20, 3, pp. 885-889 (1973)
[7] D. Sagan and D. Rubin, Linear analysis of coupled lattices, Phys. Rev. ST Accel. Beams 2, 074001 (1999)
[8] I. Borchardt, E. Karantzoulis,H. Mais, G. Ripken, DESY 87-161 (1987)
[9] V. A. Lebedev and S. A. Bogacz, Betatron motion with coupling of horizontal and vertical degrees of freedom, FERMILAB-PUB-10-383-AD (2012)
[10] R. Talman, A Proposed Möbius Accelerator, Phys. Rev. Lett. 74, 1590 (1995)
[11] A. N. Filippov et al., in proceedings of 15th Int. Conf. High Energy Accelerators, Hamburg (Germany), (1992), p.1145
[12] M. Aiba, M. Ehrlichman, and A. Streun, Round beam option in electron storage rings and generalization of Möbius accelerator, in proceedings of IPAC2015, Richmond, VA, USA (2015)
[13] V. V. Danilov et al., The Concept of Round Colliding Beams, in proceedings of EPAC96, Barcelona (1996), p.1149.
[14] S. Hendersen et al., Investigation of the Möbius accelerator at CESR, in proceedings of IPAC 1999, New York (USA) (1999)
[15] I. A. Koop, VEPP-2000 Project, arXiv:physics/0106013 [physics.acc-ph]
[16] Y. Cai, et al., Ultimate storage ring based on fourth-order geometric achromats, Phys. Rev. STAB 15, 054002 (2012)
[17] L. Farvacque et al., A low-emittace lattice for the ESRF, in proceedings of IPAC'13, Shanghai, China (2013)
[18] M. Eriksson et al., Commissioning of the MAX IV light source, in proceedings of IPAC'16, Busan, Korea (2016)
[19] S. Henderson, Status of the APS upgrade project, in proceedings of IPAC'15, Richmond, VA, USA (2015)
[20] D. Einfeld et al., A pure insertion device synchrotron light source utilizing the MBA-optics, J. Phys. IV (France) 04, C9-373 (1994)
[21] D. Einfeld et al., First multi-bend achromat lattice consideration, Journal of Synchrotron Radiation, 21, 856-661 (2014)
[22] L. C. Teng, Minimizing the Emittance in Designing the Lattice of an Electron storage Ring, Fermilab Report No. TM-1269 (1984)
[23] C. X. Wang, Minimum emittance in storage rings with uniform or nonuniform dipoles, Phys. Rev. ST Accel. Beams 12, 061001 (2009)
[24] S. Y. Lee, Emittance optimization in three- and multiple-bend achromats, Phys. Rev. E 54, 1940 (1996)
[25] K. Oide and H. Koiso, Dynamic aperture of electron storage rings with noninterleaved sextupoles, Physical Review E 47, 2010 (1993)
[26] K. Brown, A second-order magnetic optical achromat, IEEE Trans Nucl. Sci. NS-26 3490 (1979)
[27] K. Balewski et al. (eds.), Petra III : A Low Emittance Synchrotron Radiation Source, Technical Design Report, DESY (2004)
[28] W. Drube et al., The PETRA III extension, AIP Conference Proceedings 1741, 020035 (2016)
[29] R. Wanzenberg et al., Research activities towards a conversion of PETRA III into a diffraction limited synchrotron light source, in proceedings of IPAC 2017, Copenhagen, Denmark (2017)
[30] D. Einfeld et al. A Lattice Design to Reach the Theoretical Minimum Emittance for a Storage Ring, in proceedings of EPAC 1996, Barcelona, Spain (1996)
[31] Y. Jiao et al., Parameter scaling and practical design of TME lattice, SLACPUB-14205 (2010)
[32] S. Y. Lee, Accelerator Physics, 3rd edition, World Scientific Press 2012
[33] M. Sands, The physics of electron storage rings: an introduction, SLAC-R-121 (1970)
[34] J. Bengtsson, The Sextupole Scheme for the Swiss Light Source (SLS): An Analytic Approach, SLS Note 9/97 (1997)
[35] E. Forest et al., Introduction to the polymorphic tracking code : Fibre bundles, polymorphic Taylor types and "Exact tracking", KEK Report 20023 (2002)
[36] F. Schmidt, MAD-X PTC integration, in proceedings of PAC 2005, Knoxville, Tennessee (USA) (2005)
[37] M. Hénon and C. Heiles, The applicability of the third integral of motion: Some numerical experiments, The Astronomical Journal. 69: 7379 (1964)
[38] L. Emery, "Coupling of betatron motion to the longitudinal plane through path lengthening in low alpha(c) storage rings," Int. J. Mod. Phys. Proc. Suppl. A **2B** (1993) 1172
[39] Y. Shoji, Dependence of average path length betatron motion in a storage ring, PRST-AB 8, 094001 (2005)